RESEARCH ARTICLE

Terra Nova WILEY

Degassing of soil gas radon and its implication to fault activity in the western margin of the Ordos Block, China

Zhaofei Liu[1,2] | Zhi Chen[1] | Ying Li[1] | Peng Du[3] | Yuanxin Zhao[4] | Lei Lei[5] | Chang Lu[1] | Ruilin Huangfu[2,6]

[1]CEA Key Laboratory of Earthquake Prediction (Institute of Earthquake Forecasting), China Earthquake Administration, Beijing, China

[2]School of the Earth Sciences and Resources, China University of Geosciences, Beijing, China

[3]Earthquake Agency of Ningxia Hui Autonomous Region, Yinchuan, China

[4]Institute of Geochemistry, Chinese Academy of Sciences, Guiyang, China

[5]Development Research Center of China Earthquake Administration, Beijing, China

[6]SINOPEC Henan Oilfield Branch Company, Nanyang, Henan, China

Correspondence
Ying Li, CEA Key Laboratory of Earthquake Prediction (Institute of Earthquake Forecasting), China Earthquake Administration, Beijing 100036, China.
Email: liying@ief.ac.cn

Abstract

Soil gas radon (Rn) serves as an effective indicator for assessing fault activity in fault zones. Measurement of Rn degassing at the active faults was conducted twice in 2017 and 2018 to assess fault activity in the western margin of the Ordos block. The concentration and flux values of Rn ranged from 0.41 to 40.93 kBq m^{-3} and 5.17 to 140.33 mBq m^{-2} s^{-1}, respectively. The compression of the Tibetan Plateau has led to higher Rn concentration and flux in the southern part compared with the northern part. The fault activity is evaluated by the index of I_{Rn} calculated from Rn concentrations. The Haiyuan arcuate tectonic region exhibited the most intensive fault activity, followed by the Yinchuan Basin and Jilantai-Linhe Basin. These findings enhance our understanding of the relationship between fault activity and Rn emission and provide a significant geochemical reference for the fault activity.

KEYWORDS
fault activity, gas geochemistry, soil gas radon, the western margin of the Ordos block

1 | INTRODUCTION

The active fault system, along with its associated fractures at the block boundary, plays a fundamental role in serving as the preferred pathway for the propagation of deep gas (Caracausi & Sulli, 2019; Sano et al., 2017; Xu et al., 2017; Zheng et al., 2017). Through rock loading experiments, it has been determined that amplified radon (Rn) emissions from broken rocks can be attributed to the increased presence of fractures (Chen et al., 2019; Toutain et al., 1992; Tuccimei et al., 2010). Field measurements and monitoring have further

demonstrated that the spatial and temporal variations of soil gas Rn concentrations and fluxes in active fault zones are closely linked to fault activity (Fu et al., 2017; Wang et al., 2014; Yang et al., 2018). Notably, Rn gas anomalies have been observed prior to numerous seismic events, indicating their potential as precursors (e.g., Igarashi et al., 1995; Martinelli, 2020; Ülküm et al., 2018; Zhou et al., 2016).

The tectonic and seismic activities in the study area have garnered significant attention due to the presence of large-scale faults and intense seismic events. From 1125 to 1954, the area experienced 8 earthquakes of $M_S \geq 7.0$ and 2 earthquakes with $M_S \geq 8.0$

(Wesnousky et al., 1984). Geophysical investigations have indicated that the area is a critical area of potential seismic risk (Liu et al., 2016; The Research Group on "Active Fault System around Ordos Massif", State Seismological Bureau (SSB), 1988). Furthermore, analysis of GPS velocity fields spanning from 1999 to 2015 in North China has revealed an increasing migration rate (Gao et al., 2016). Additionally, it has been suggested that the 2008 Wenchuan M_S 8.0 earthquake may have enhanced the seismicity around the Ordos block (Gao et al., 2016; Zhu et al., 2010).

The soil gas geochemistry in the study area has been investigated by several researchers (Cui et al., 2019; Meng et al., 1997; Sun et al., 2016). Cui et al. (2019) have demonstrated a significant relationship between tectonic activity and soil gas CH_4 and CO_2 emissions from the boundary of the blocks in the study area. Meng et al. (1997) conducted measurements of soil gas Rn and Hg in the Haiyuan arcuate tectonic region and identified a clear positive correlation between soil gas concentrations and fault activity. Sun et al. (2016) observed higher concentrations of soil gas Rn near the epicentre of the 1920 M_S 8.5 Haiyuan earthquake compared to other areas, as well as a significant contribution of mantle-sourced helium from nearby hot springs. However, most of these studies have focused on specific regions, leading to limited understanding in large areas with diverse active faults. This study comprehensively analyses the correlation between Rn emissions and regional tectonic activity in the western margin of the Ordos block. Through Rn concentration and flux measurements, we investigate the complex relationship between Rn emissions and various factors. Our findings enhance our understanding of Rn degassing, fault properties and slip rates. Additionally, our research contributes to seismic risk assessment and the development of effective earthquake prediction and mitigation strategies.

2 | GEOLOGICAL SETTINGS

The western margin of the Ordos block is situated in northern Central China (Figure 1). The collision between the Indian plate and the Eurasian plate has resulted in the convergence of the Tibetan Plateau and the North China craton in the southwestern part of the Ordos block (The Research Group on "Active Fault System around Ordos Massif", State Seismological Bureau (SSB), 1988; Yin & Harrison, 2000). This collision has given rise to distinct movement patterns among the blocks in the study area. Specifically, the Lanzhou block and Haiyuan block exhibit clockwise rotation at rates of 17.17 nanostrain·a^{-1} and 4.69 nanostrain·a^{-1}, respectively. Conversely, the Ordos block and Minqin block display counterclockwise rotation at rates of 9.07 nanostrain·a^{-1} and 2.89 nanostrain·a^{-1}, respectively. In terms of movement rates, the Lanzhou block demonstrates a higher rate of 8.4 mm·a^{-1}, followed by the Haiyuan block with a medium rate of 5.0 mm·a^{-1}. The Ordos and Minqin blocks exhibit lower rates of 2.8 mm·a^{-1} and 2.2 mm·a^{-1}, respectively (Wang et al., 2017). The different movement patterns of these blocks resulted in the formation of 11 major active faults, with Holocene slip rates ranging from 0.14 to 5.29 mm·a^{-1} (Table S1).

Significance Statement

Radon (Rn) is a radioactive gas that originates from the natural decay of other radioactive elements present in rocks in Earth's crust. In fault zones, soil gas Rn serves as an effective indicator for assessing fault activity. In this study, we examined the spatial distribution of Rn concentration and flux in the compression and tension zones between the Tibetan Plateau and the Ordos block for the first time and used Rn concentration to assess activity levels of 11 faults. Our findings indicate that Rn concentration and flux are higher in the southern part of the study area due to the accumulation of strain, which favours the formation of fractures and enhances Rn migration. Fault activity is evaluated using an index of I_{Rn}, calculated from Rn concentration. There is a positive correlation between I_{Rn} and the Holocene slip rate of the fault. Compression of the Tibetan Plateau results in higher I_{Rn} in the southern part of the study area than in the northern part.

Due to differences in movement directions, rates of block movements, and stress status, the western margin of the Ordos Block has been divided into three regions (Geological Bureau of Ningxia (GBN), 1976; The Research Group on "Active Fault System around Ordos Massif", State Seismological Bureau (SSB), 1988; Wang et al., 2017; Yin & Harrison, 2000). The Haiyuan arcuate tectonic region (HATR) is characterized by compression, while the Yinchuan Basin (YB) and Jilantai-Linhe Basin (JLB) exhibit extensional tectonics (Ningxia Bureau of Geology and Mineral Resources (NBGMR), 1989; The Research Group on "Active Fault System around Ordos Massif", State Seismological Bureau (SSB), 1988; Zhang et al., 2019). The HATR is characterized by the presence of four strike-slip and thrust faults (GF, XTF, YF and LNF). These faults are formed due to the obstruction of the northeast-trending movement of the Tibetan Plateau by the stable Alxa and Ordos blocks (The Research Group on "Active Fault System around Ordos Massif", State Seismological Bureau (SSB), 1988). In YB, an active Cenozoic graben, under the influence of NW–SE extensional stress, a dextral strike-slip and thrust fault (HWF) and a series of NE-trending normal active faults (e.g., YRF and HEF) have developed (Ningxia Bureau of Geology and Mineral Resources (NBGMR), 1989). The JLB, composed of the Jilantai basin and Linhe basin, is a Cenozoic extensional graben where four normal faults (BFF, ZWF, LFF, and SFF) have formed (Geological Bureau of Ningxia (GBN), 1976; The Research Group on "Active Fault System around Ordos Massif", State Seismological Bureau (SSB), 1988). These unique tectonic settings have given rise to significant seismic events, including the M_S 8.5 Haiyuan earthquake (16 December 1920), which is the largest recorded inland earthquake. Additionally, six earthquakes with magnitudes of $6.0 \leq M_S \leq 6.9$ and two earthquakes with magnitudes $M_S \geq 7.0$ have occurred in the vicinity.
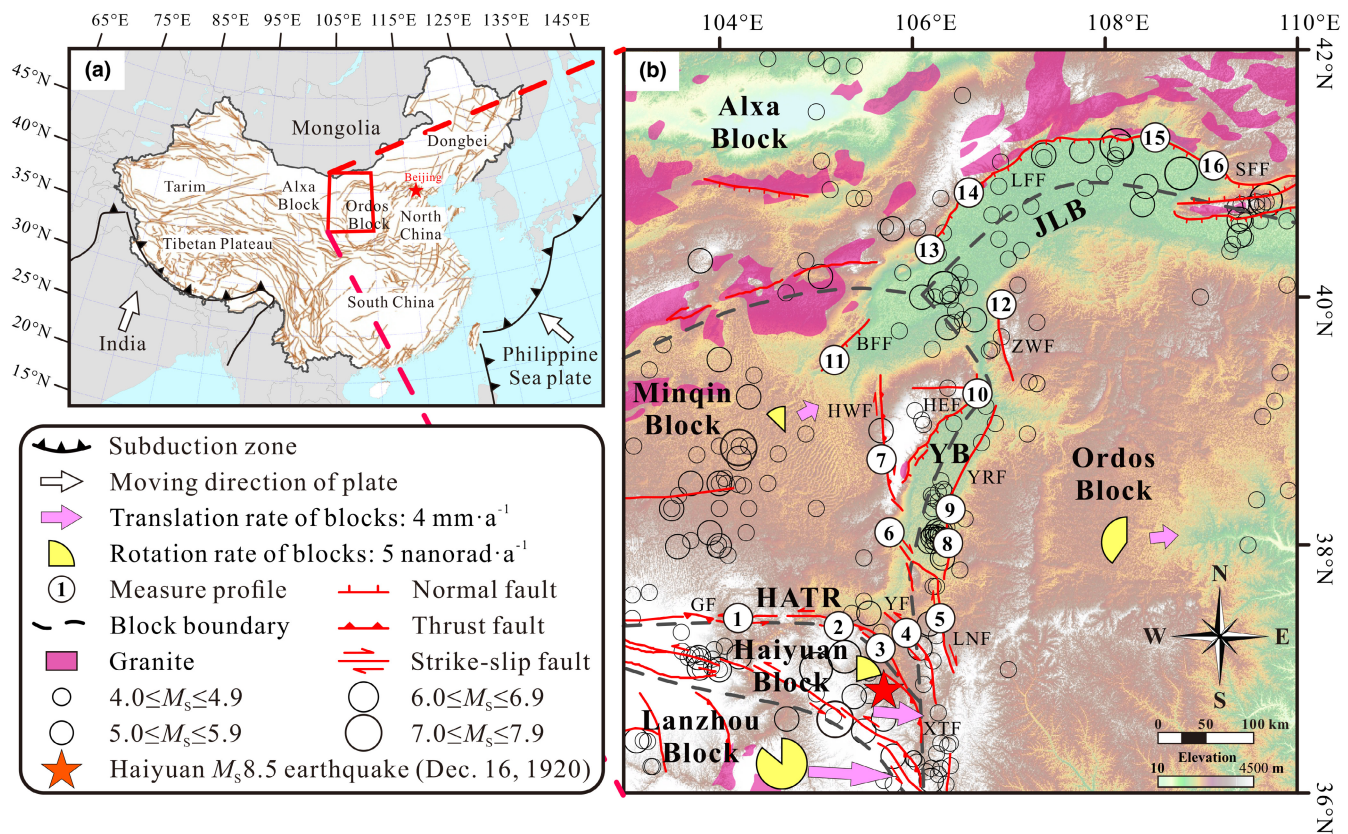
FIGURE 1 (a) The location of the study area in China. (b) The tectonic map of the study area (modified from Wang et al., 2017). The yellow sector symbol denotes the rotation rate of the block, with a quarter sector indicates a rate of 5 nanorod·y⁻¹. The rotation direction of the sector denotes the rotation direction of the block. The pink arrow denotes the direction of the block movement, with the length of the arrow indicating the speed of plate movement. The abbreviations are as follows: BFF, Bayanwulashan frontal fault; GF, Guanguanling fault; HATR, the Haiyuan arcuate tectonic region; HEF, Helanshan East-piedmont fault; HWF, Helanshan West-piedmont fault; JLB, the Jilantai-Linhe Basin; LFF, Langshan frontal fault; LNF, Luoshan–Niushoushan fault; SFF, Sertengshan frontal fault; XTF, Xiangshan–Tianjingshan fault; YB, the Yinchuan Basin; YF, Yantongshan fault; YRF, Yellow River fault; ZWF, Zhuozishan West-piedmont fault. Earthquake data were recorded between 16 December 1920 and 31 December 2018 (https://data.earthquake.cn/). Fault data are sourced from Deng et al. (2003). Geological map modified from Ma et al. (2002). The DEM data set is provided by the Geospatial Data Cloud site, Computer Network Information Center, Chinese Academy of Sciences (http://www.gscloud.cn).

3 | RESULTS

In this study, a total of 701 concentration sampling points and 96 flux sampling points were measured twice in 16 profiles across 11 active faults in the western margin of the Ordos block in 2017 and 2018. For detailed information regarding the measurement methods and statistical analysis, please refer to Data S1. The Rn concentration and flux in the study area exhibit a wide range of variation (Table S2). The Rn concentrations range from 0.41 to 40.93 kBq·m⁻³; the fault-origin Rn concentrations (H_{Rn}) range from 2.26 to 35.37 kBq·m⁻³; and the background values (L_{Rn}) range from 1.69 to 13.01 kBq·m⁻³. The values of I_{Rn}, calculated as H_{Rn} divided by L_{Rn} (Chen et al., 2018), range from 1.27 to 3.62. The Rn fluxes range from 5.17 to 140.33 mBq·m⁻²s⁻¹, with the highest Rn flux values above 100 mBq·m⁻²s⁻¹ in profiles No. 1 and No. 5. The correlation coefficients (Pearson's r) for Rn concentration between the two surveys is 0.94, while the correlation coefficients (Pearson's r) for Rn flux is 0.88. This means of Rn concentration/flux from the 16 profiles in 2 years are similar.

A total of 16 soil samples were collected from each profile, and the contents of radioactive materials (U, Th and Ra) from soil samples have been analysed (Table S3). The highest values of U content and Ra content were observed in profile No. 3, which are 43.7 and 37.9 Bq·kg⁻¹, respectively. The highest value of Th content was observed in profile No. 14, which is 52.7 Bq·kg⁻¹.

4 | DISCUSSION

4.1 | Spatial distribution characteristics and influencing factors

The spatial distribution of Rn concentrations and fluxes (Figure 2a,b) reveals that high levels are predominantly found in HATR and YB. Additionally, the southern part of the study area exhibits higher Rn emissions compared to the northern part. Various factors such as fault activity, rock types, radioactive material contents (U, Th and Ra), vegetation and meteorological conditions are likely to influence

Rn emissions in the fault zones (Han et al., 2014; Papp et al., 2008; Winkler et al., 2001).

The study area is a transition zone with arid and semiarid continental climates (The Research Group on "Active Fault System around Ordos Massif", State Seismological Bureau (SSB), 1988). It consists mostly of gobi and desert landscapes with limited rainfall and vegetation (Figure 2c). No rainfall events were recorded during the measurement period. The Pearson correlation analysis was conducted to examine the relationship between meteorological conditions and the mean values of Rn concentration and flux of each profile in two surveys. The results indicate a weak correlation between meteorological conditions, including atmospheric pressure, air temperature, soil temperature and temperature difference, and Rn concentration and flux (Table 1). The Pearson's r values range from −0.57 to 0.39 (Figures S3 and S4). Therefore, meteorological conditions and vegetation are not expected to exert considerable influence on the emission of soil gas Rn in this study.

Rn emissions are typically high in granite, followed by shale, limestone and sandstone (Baixeras et al., 2001; El-Arabi et al., 2006). In Figure 2d, it can be observed that granites are extensively exposed in the northwest margin of the JLB, particularly near profiles No. 11 to No. 16. However, high concentrations and fluxes of Rn are only observed in profile No. 11, with elevated Rn concentrations also observed in profile No. 14. Interestingly, most of the high concentrations and fluxes occur in profiles No. 1 to No. 9, where there are no granite outcrops. This observation suggests that there is no correlation between rock types and Rn emissions within the study area.

Furthermore, the correlation between the contents of radioactive materials (U, Th and Ra) and soil gas Rn was also analysed (Table 1). The correlation coefficients (Pearson's r) between the contents of radioactive materials and Rn fluxes ranged from 0.11 to 0.32 (Figures S3 and S4), indicating a weak correlation. The content of Ra and Th showed exhibited a positive correlation with Rn concentration, with correlation coefficients ranging from 0.47 to 0.54. This suggests that the Rn background is influenced to some extent by the content of Ra and Th in the local soil. In other words, the source of soil gas Rn comes partly from soil.

The Rn concentration along the profiles tends to be higher near the fault planes. This trend is observed in most of the 16 profiles (excluding profiles 6, 13, 14 and 16) (Figure S5). These variations in Rn concentration can be attributed to changes in permeability resulting from fault activity (Faulkner et al., 2010; Yang et al., 2018). It is speculated that the release of Rn from the fault zones originates from underground sources. Increased fault activity can result in the formation of new fractures or the opening of preexisting fractures, providing pathways for the release of Rn and subsequently leading to a significant increase in Rn emission rates (Mollo et al., 2011; Nicolas et al., 2015; Roeloffs, 1999). This study verifies a clear positive correlation between the fault-origin Rn concentration (H_{Rn}) and the Holocene slip rate of the faults, with correlation coefficients of 0.51 and 0.66 in the two surveys (Figure 3a). These findings suggest that fault activity plays a significant role in influencing the emission of Rn in the study area.

A previous study conducted by our research group has shown that the concentrations of CH_4 and CO_2 increased as the strike-slip rate across the faults increased, with significantly higher concentrations observed in the southern part of the western margin of the Ordos Block compared to the northern part (Cui et al., 2019). Considering the similarities in the spatial distribution of Rn concentration, it is reasonable to speculate that CH_4 and CO_2 may be the carrier gases for the upward migration of Rn.

The HATR serves as a transitional zone between the Tibetan Plateau and the Ordos block. The presence of abnormally high-shear strain rate (Figure 2b), crustal horizontal strain rate (Figure 2c), and the steepest gradient of GPS horizontal velocity (Figure 2d) indicates the intense deformation of the crust in HATR. This deformation is primarily attributed to the northeastward extrusion pressure exerted by the Tibetan Plateau and the resistance offered by the Ordos block. Consequently, a series of earthquakes occurred within the HATR, leading to the formation of numerous seismic rupture zones in the southern part of the study area (Figure 2a). The high permeability of the rupture zones in the southern part also contributes to higher concentrations and fluxes of Rn compared to the northern part. The influence of compression from the Tibetan Plateau gradually diminishes in the YB and JLB. The GPS horizontal velocity field indicates that the Ordos block, Alxa block and Minqin block exhibit relative stability. This stability is the main reason for the lower Rn concentration and flux observed in the YB and JLB (profiles No. 10 to No. 16). However, profiles No. 8 and No. 9, located in the YB, still exhibit high-Rn concentrations. These profiles are situated along the YRF, where the Pingluo M_8 earthquake occurred (Lei, 2016). In seismic rupture zones, the convective velocity of Rn has been estimated to range from 5.2 to 28.0 m·d^{-1}, disregarding carrier gas and diffusion effects (Miklyaev et al., 2020). The YRF has exhibited frequent seismic activity in recent years, which has likely promoted the migration of Rn (Figure 4). In conclusion, the movement of blocks and seismic activity are the main factors contributing to the higher Rn emissions in the southern part compared to the southern part.

4.2 | Fault activity assessment

In this study, the index of I_{Rn}, calculated as the ratio of fault-origin Rn concentration (H_{Rn}) to background value (L_{Rn}), has been used to evaluate fault activity (Table S2). Although the Rn concentration/flux in the two surveys were similar, there were still some differences between them. Both measurements were conducted in the same season, minimizing the influence of meteorological factors. Moreover, no significant large seismic event was recorded before and after the surveys. Yuce et al. (2017) attributed the differences in soil gases between the two surveys in 2013 and 2014 to changes in permeability resulting from crustal deformation. The difference between the two surveys in this study may also be due to crustal deformation. To ensure accuracy, the average I_{Rn} in two surveys is used for fault activity assessment.
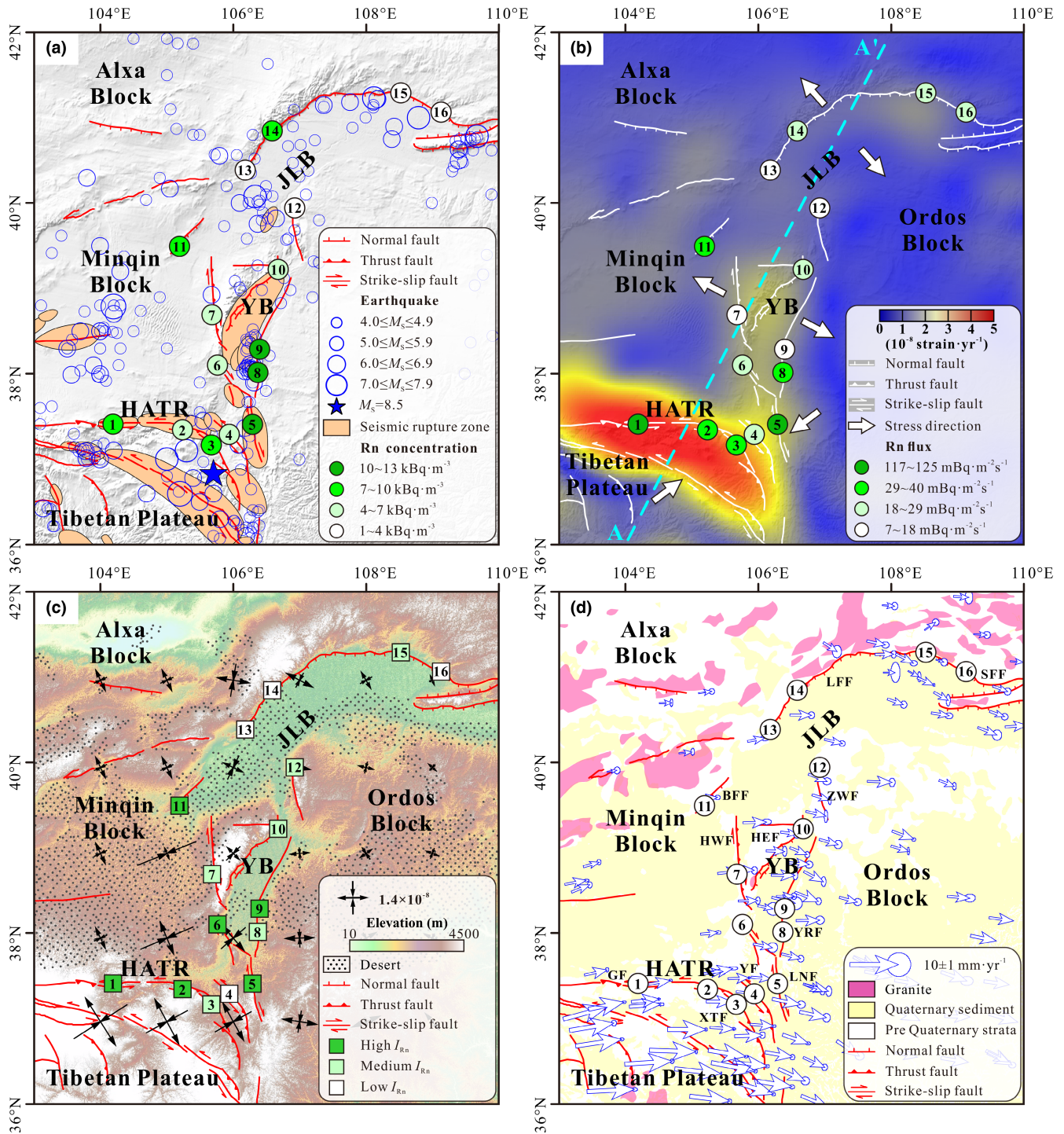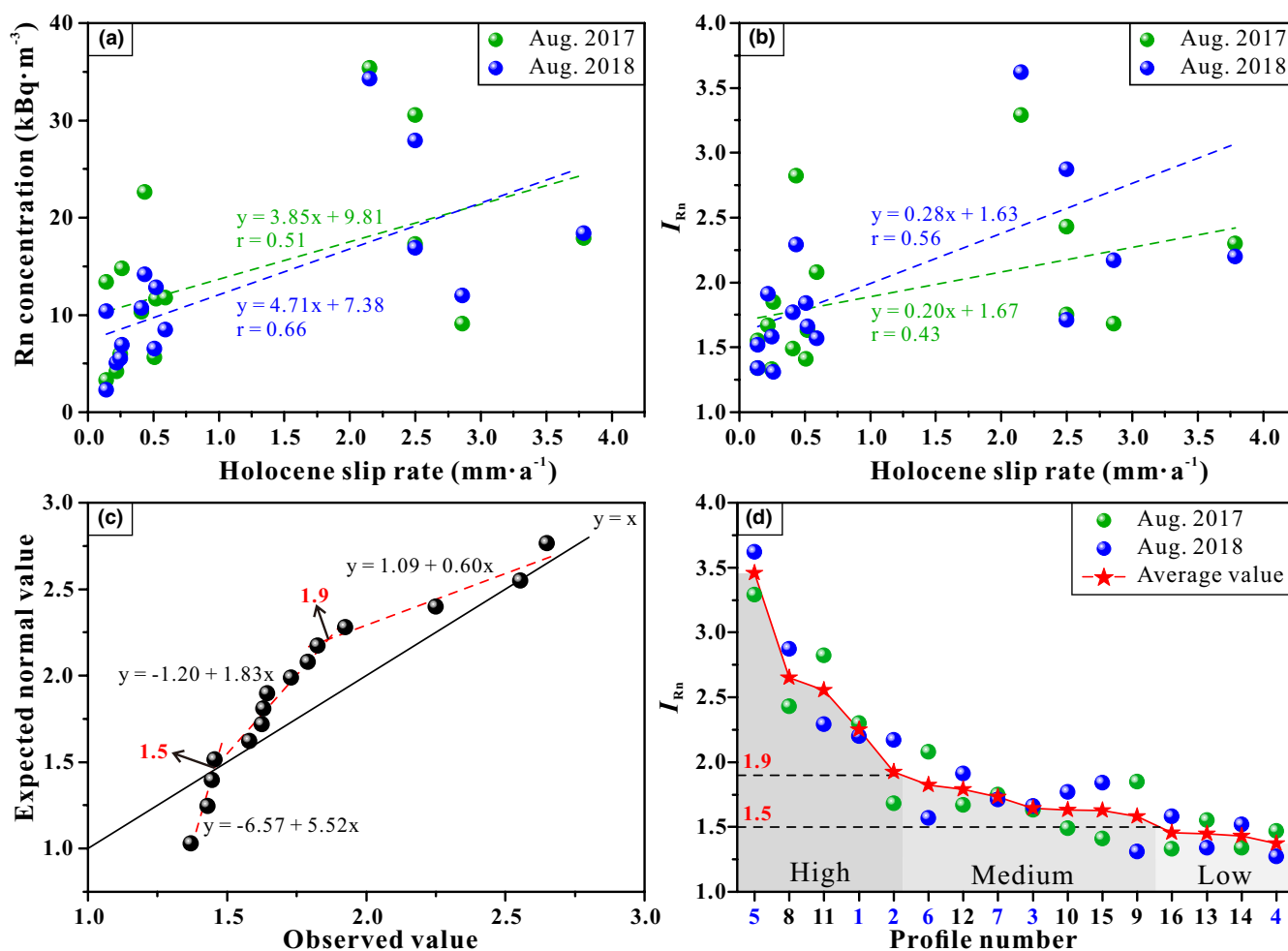
FIGURE 2 (a) Distribution of Rn concentration and locations of earthquakes. Earthquakes were recorded in the period of 16 December 1920~31 December 2018 (https://data.earthquake.cn/). Locations of seismic rupture zone modified from Working Group of M7 (2012). (b) Distribution of Rn flux and shear strain rate (Li, Li, & Zhou, 2018). (c) Distribution of I_{Rn} and crustal horizontal strain rate (Li, Liu, et al., 2018); Geographical location of the desert (modified from Ma et al., 2002). (d) The GPS horizontal velocity field around the Ordos block with respect to the stable Eurasian reference frame, and the error ellipses represent 95% confidence (Zhao et al., 2017). The geological map was modified from Ma et al. (2002). Abbreviations are shown in Figure 1. Fault data are quoted from Deng et al. (2003). The DEM data set is provided by the Geospatial Data Cloud site, Computer Network Information Center, Chinese Academy of Sciences. (http://www.gscloud.cn).

TABLE 1 The correlation coefficients (Pearson's r) between Rn concentration and flux, the content of radioactive materials (U, Th and Ra) from soil samples and meteorological conditions.

Pearson's r	Rn concentration (kBq m^{-3})		Rn flux (mBq m^{-2} s^{-1})	
	Aug. 2017	Aug. 2018	Aug. 2017	Aug. 2018
$P_{Atm.}$ (Pa)	−0.17	−0.29	−0.57	−0.55
T_{air} (°C)	0.14	0.05	−0.24	−0.09
T_{soil} (°C)	−0.42	−0.32	−0.33	−0.24
ΔT (°C)	0.39	0.27	−0.05	0.07
C_U (Bq·kg^{-1})	0.25	0.27	0.16	0.11
C_{Th} (Bq·kg^{-1})	0.52	0.47	0.15	0.18
C_{Ra} (Bq·kg^{-1})	0.47	0.54	0.22	0.32

Note: $P_{Atm.}$ is the atmospheric pressure; T_{air} is the air temperature; T_{soil} is the soil temperature; ΔT is the difference between air temperature and soil temperature ($\Delta T = T_{air} - T_{soil}$).

The positive relationship between I_{Rn} and the Holocene slip rate of the faults in 2017 and 2018, with a correlation coefficient of 0.56 and 0.43, respectively (Figure 3b), confirms the reliability of using I_{Rn} for assessing fault activity in the study area. The Q–Q plots of average I_{Rn} in 2 years exhibit three linear segments (Figure 3c), and the two intersections determine the boundaries of I_{Rn}. Consequently, the I_{Rn} values for all profiles are divided into three groups representing different levels of Rn activity: high ($I_{Rn} > 1.9$), medium ($1.9 > I_{Rn} > 1.5$) and low ($I_{Rn} < 1.5$) Rn activity (Figure 3d).

The spatial distribution of shear strain rate, determined using GPS and precise levelling data, demonstrates a gradual decrease from the southern part to the northern part (Li, Liu, et al., 2018). This trend is also observed in the distribution of I_{Rn} (Figures 2b and 5). The highest level of fault activity is observed in the HATR, followed by the YB, and then the JLB. Except for profile No. 4, most of the profiles on the thrust faults exhibit higher I_{Rn} than the normal faults. This observation suggests that the fault activity in the compressional zone of the study area is stronger than in the extensional zone.
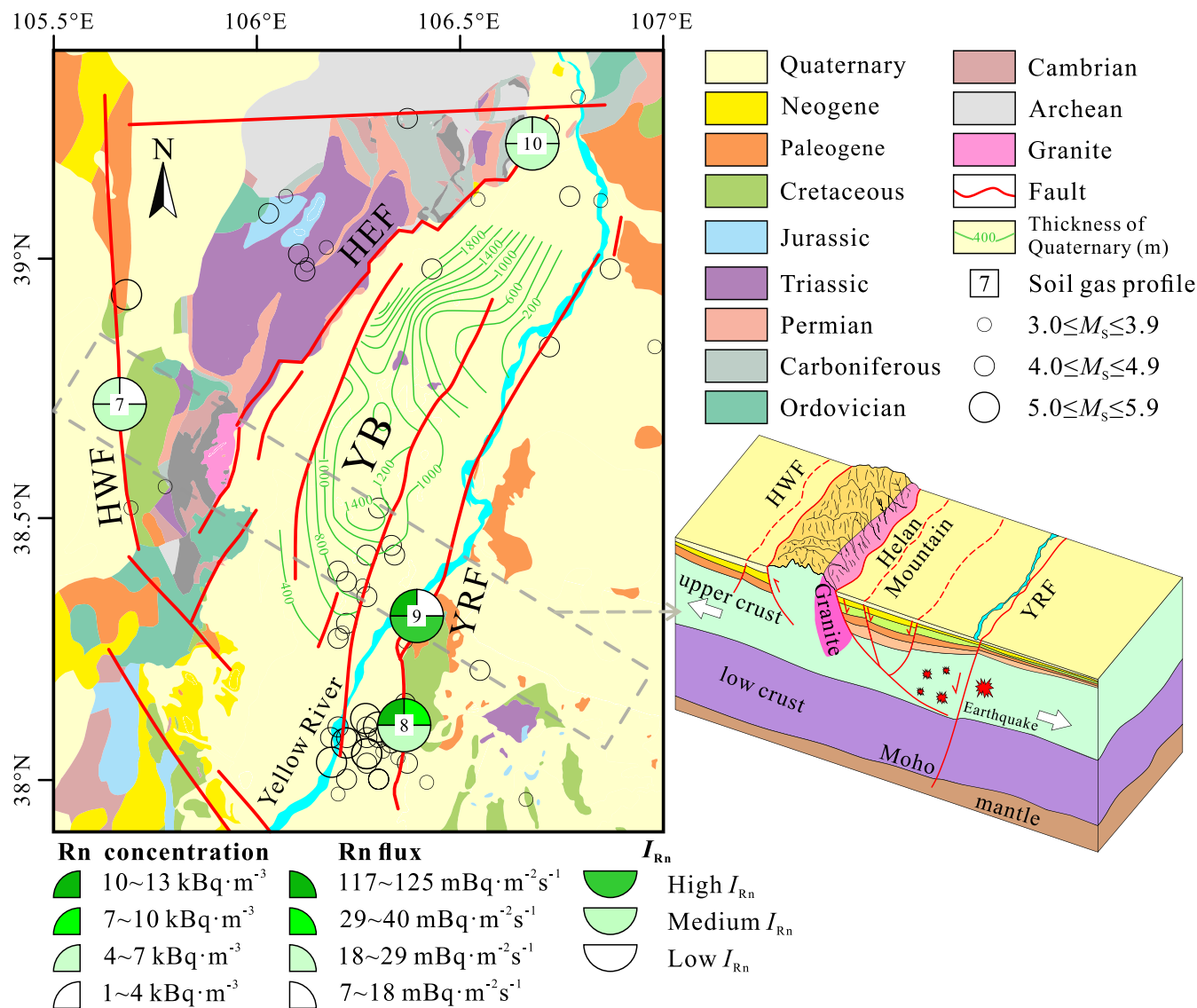

FIGURE 3 (a) The correlation coefficients between the Holocene slip rate of fault and fault-origin Rn concentration (H_{Rn}) in two surveys. (b) The correlation coefficients between the Holocene slip rate of the fault and I_{Rn} in two surveys. (c) Quantile-quantile plots (Q-Q plots) of I_{Rn}. (d) I_{Rn} of the fault zones in the western margin of the Ordos block. Abbreviations are shown in Figure 1. The profiles from thrust faults are marked in blue, and the profiles from normal faults are marked in black.

FIGURE 4 Geological map of the YB. Earthquakes were recorded in the period of 16 Decemeber 1920~31 December 2018 (https://data.earthquake.cn/). Abbreviations are shown in Figure 1. Fault data are quoted from Deng et al. (2003). Geological map modified from Ma et al. (2002).

These findings provide further evidence of the dominant influence of tectonic stress on Rn emissions.

The most active faults in the study area are identified as GF (No. 1), XTF (No. 2), LNF (No. 5), YRF (No. 8) and BFF (No. 11) (Figure 2d). Among these, the highest I_{Rn} value (up to 3.62) is observed in LNF, which is comparable to the I_{Rn} value of the Tangshan fault, the seismogenic fault of the 1976 Tangshan M_S 7.8 earthquake (3.90, Chen et al., 2018). The GF, XTF and LNF are located in the HATR, which serves as a transitional zone between the Tibetan Plateau and the Ordos block (Figure 1). A gradual decrease in crustal thickness from south to north can be observed in Figure 5. Additionally, the V_S of the crust in HATR is significantly lower compared to YB and JLB. This can be attributed to the expansion of the northeastern margin of the Tibetan Plateau since the Cenozoic era, resulting in the fragmentation of the upper crust (Zheng et al., 2018). This region experiences ongoing tectonic compression and intense seismic activity, including the Haiyuan M_S 8.5 earthquake and three earthquakes with magnitudes above 7.0 (Gao et al., 2016). Therefore, block movements and seismic activity are responsible for the strong fault activity and high-Rn concentration and flux in the area. The YRF is the seismogenic fault responsible for one M_S 8.0 earthquake and two M_S 6.5 earthquakes (Huang et al., 2016; The Research Group on "Active Fault System around Ordos Massif", State Seismological Bureau (SSB), 1988). Seismic activity is a visual manifestation of tectonic movement, and the frequent seismic activity near the YRF indicates strong fault activity (Figure 4). And high-Rn concentrations and fluxes are also observed in the YRF. BFF is situated at the junction of the Alxa block and Minqin block. The differential movement between these blocks may contribute to the high I_{Rn} observed in profile No. 11.
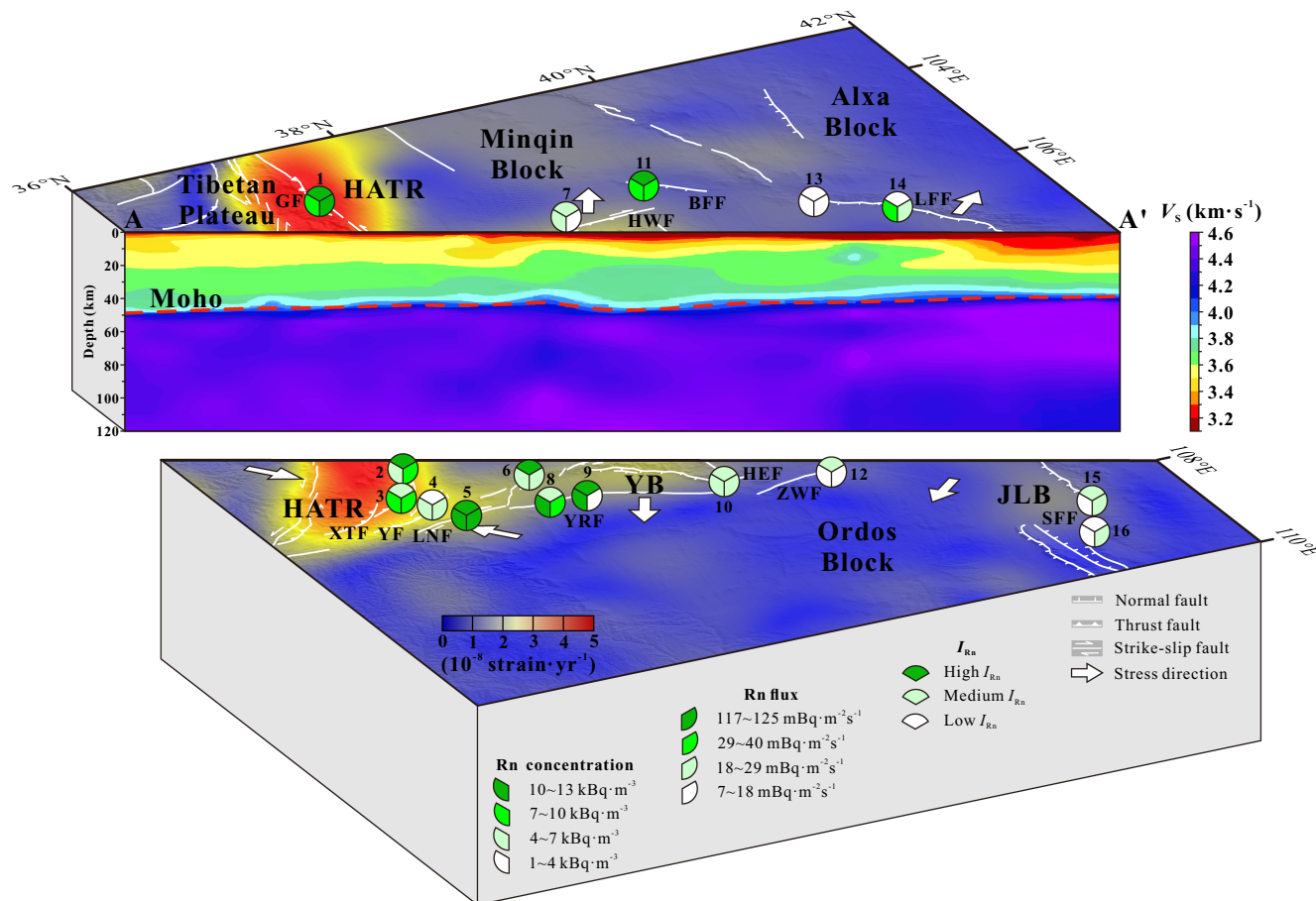
FIGURE 5 A model map of the study area. Crustal horizontal strain rate modified from Li, Li, and Zhou (2018). Vertical cross-section of shear wave velocity (Vs) modified from Zheng et al. (2018). The location of the vertical cross-section is shown in Figure 2b. Abbreviations are shown in Figure 1. Fault data are quoted from Deng et al. (2003). Geological map modified from Ma et al. (2002).

5 | CONCLUSION

This study provides valuable insights into the dominant influence of fault activity on Rn emission in the western margin of the Ordos block. Through the analysis of 701 concentration sampling points and 96 flux sampling points, it was observed that the concentration and flux of Rn varied across different profiles and regions, with higher emissions observed in the southern part of the study area. It was also found that rock type and meteorological condition had limited effects on Rn emission. The index of Rn concentrations (I_{Rn}) was used to evaluate fault activity, revealing that the faults in the Haiyuan arcuate tectonic region exhibited the most intensive activity, followed by those in the Yinchuan Basin and the Jilintai-Linhe Basin. This pattern of fault activity aligns well with the shear strain rates. Notably, the Guanguanling fault, Xiangshan–Tianjingshan fault, Luoshan–Niushoushan fault, Yellow River fault and Bayanwulashan frontal fault were identified as the most active faults in the study area. The study's results provide a valuable geochemical reference for assessing fault activity and have significant implications for seismic hazard assessment and earthquake prediction in the region. Additionally, this study deepens our understanding of the relationship between fault activity and Rn emission. These findings can be applied to improve seismic hazard models and aid in mitigating earthquake-related disasters.

DATA AVAILABILITY STATEMENT

Radon data can be found at Mendeley Data, V1 (https://doi.org/10.17632/pp9fskxxbh.1). The data of Rn in 2017 is quoted from Liu et al. (2023). The data of Rn in 2018 is quoted from Chen et al. (2022).

DECLARATION OF INTEREST STATEMENT

For the manuscript "Degassing of soil gas radon and its implication to fault activity in the western margin of the Ordos Block, China", by Liu et al., all co-authors have seen and agree with the contents of the manuscript and there is no financial interest to report. We certify that the submission is an original work and is not under review for any other publication.

REFERENCES

Baixeras, C., Erlandsson, B., Font, L., & Jönsson, G. (2001). Radon emanation from soil samples. *Radiation Measurements*, *34*, 441–443. https://doi.org/10.1016/s1350-4487(01)00203-7

Caracausi, A., & Sulli, A. (2019). Outgassing of mantle volatiles in compressional tectonic regime away from volcanism: The role of continental delamination. *Geochemistry, Geophysics, Geosystems*, *20*, 2007–2020. https://doi.org/10.1029/2018GC008046

Chen, Z., Li, Y., Liu, Z., He, H., Martinelli, G., Lu, C., & Gao, Z. (2022). Geochemical and geophysical effects of tectonic activity in faulted areas of the North China craton. *Chemical Geology*, *609*, 121048. https://doi.org/10.1016/j.chemgeo.2022.121048

Chen, Z., Li, Y., Liu, Z. F., Wang, J., Zhou, X. C., & Du, J. G. (2018). Radon emission from soil gases in the active fault zones in the Capital of China and its environmental effects. *Scientific Reports*, *8*(16772), 1–12. https://doi.org/10.1038/s41598-018-35262-1

Chen, Z., Li, Y., Liu, Z. F., Zheng, G. D., Xu, W., Yan, W., & Yi, L. (2019). CH_4 and CO_2 emissions from mud volcanoes on the southern margin of the Junggar Basin, NW China: Origin, output, and relation to regional tectonics. *Journal of Geophysical Research: Solid Earth*, *124*, 1–15. https://doi.org/10.1029/2018jb016822

Cui, Y. J., Li, Y., Si, X. Y., Yang, L. X., Liu, Z. F., Sun, F. X., Li, X. Y., Zheng, H. W., & Du, J. G. (2019). Tectonic controls on near-surface variations in CH_4 and CO_2 concentrations along the northwestern margin of the Ordos block, China. *Geofluids*, *2019*, 1–10. https://doi.org/10.1155/2019/7909483

Deng, Q. D., Zhang, P. Z., Ran, Y. K., Yang, X. P., Min, W., & Chu, Q. Z. (2003). Basic characteristics of active tectonics of China. *Science in China, Series D: Earth Sciences*, *46*, 356–372.

El-Arabi, A. M., Abbady, A., Ahmed, N. K., Michel, R., El-Kamel, A. H., & Abbady, A. G. E. (2006). Assessment of radon-222 concentrations and exhalation rates of rocks and building materials. *Indian Journal of Pure and Applied Physics*, *44*(4), 287–291.

Faulkner, D. R., Jackson, C. A. L., Lunn, R. J., Schlische, R. W., Shipton, Z. K., Wibberley, C. A. J., & Withjack, M. O. (2010). A review of recent developments concerning the structure, mechanics and fluid flow properties of fault zones. *Journal of Structural Geology*, *32*, 1557–1575. https://doi.org/10.1016/j.jsg.2010.06.009

Fu, C. C., Yang, T. F., Tsai, M. C., Lee, L. C., Liu, T. K., Walia, V., Chen, C. H., Chang, W. Y., Kumar, A., & Lai, T. H. (2017). Exploring the relationship between soil degassing and seismic activity by continuous radon monitoring in the Longitudinal Valley of eastern Taiwan. *Chemical Geology*, *469*, 163–175. https://doi.org/10.1016/j.chemgeo.2016.12.042

Gao, L., Hou, D., Li, J., Li, S., Dai, Y., Xiong, F., & Yang, H. (2016). Movement characteristics and present seismic activity of Ordos block. *Geodesy and Geodynamics*, *7*(6), 451–458. https://doi.org/10.1016/j.geog.2016.07.008

Geological Bureau of Ningxia (GBN). (1976). *Areal geological survey report for Jilantai area* (pp. 1–99). Geological Publishing House.

Han, X., Li, Y., Du, J., Zhou, X., Xie, C., & Zhang, W. (2014). Rn and CO_2 geochemistry of soil gas across the active fault zones in the capital area of China. *Natural Hazards and Earth System Science*, *14*(10), 2803–2815. https://doi.org/10.5194/nhess-14-2803-2014

Huang, X., Feng, S., Gao, R., & Li, W. (2016). High-resolution crustal structure of the Yinchuan basin revealed by deep seismic reflection profiling: Implications for deep processes of basin. *Earthquake Science*, *29*(2), 83–92. https://doi.org/10.1007/s11589-016-0148-1

Igarashi, G., Saeki, S., Takahata, N., Sumikawa, K., Tasaka, S., Sasaki, Y., Takahashi, M., & Sano, Y. (1995). Ground-water radon anomaly before the Kobe earthquake in Japan. *Science*, *269*(5520), 60–61. https://doi.org/10.1023/A:1004366724773

Lei, Q. Y. (2016). *The extension of the arc tectonic belt in the northeastern margin of the Tibet plateau and the evolution of the Yinchuan basin in the western margin of the North China* (pp. 1–191). Institute of Geology, China Earthquake Administration.

Li, S., Li, C., & Zhou, Q. (2018). Kinematic analysis of the Ordos block and surrounding area based on GPS data: An initiative-passive vortex structure model. *Arabian Journal of Geosciences*, *11*, 627. https://doi.org/10.1007/s12517-018-3980-x

Li, Y., Liu, M., Wang, Q., & Cui, D. (2018). Present-day crustal deformation and strain transfer in northeastern Tibetan plateau. *Earth and Planetary Science Letters*, *487*, 179–189. https://doi.org/10.1016/j.epsl.2018.01.024

Liu, J., Xie, F., & Lv, Y. (2016). Seismic hazard assessments for the Ordos block and its periphery in China. *Soil Dynamics and Earthquake Engineering*, *84*(1), 70–82. https://doi.org/10.1016/j.soildyn.2016.02.007

Liu, Z., Li, Y., Chen, Z., Zhao, Z., Huangfu, R., Zhao, Y., Lei, L., & Lu, C. (2023). Environmental impacts of ^{222}Rn, Hg and CO_2 emissions from the fault zones in the western margin of the Ordos block, China. *Environmental Geochemistry and Health*, *45*, 457–472. https://doi.org/10.1007/s10653-022-01350-5

Ma, L. F., Qiao, X. F., Min, L. R., Fa, B. X., & Ding, X. Z. (2002). *Geological atlas of China* (pp. 1–348). Geology Press.

Martinelli, G. (2020). Previous, current, and future trends in research into earthquake precursors in geofluids. *Geosciences*, *10*(189), 1–21. https://doi.org/10.3390/geosciences10050189

Meng, G., He, K., Ban, T., & Jiao, D. (1997). Study of the activity and segmentation of active faults using measurements of radon and mercury gases. *Earthquake Research in China*, *11*(3), 255–264.

Miklyaev, P. S., Petrova, T. B., Marennyy, A. M., Shchitov, D. V., Sidyakin, P. A., Murzabekov, M. A., & Lopatin, M. N. (2020). High seasonal variations of the radon exhalation from soil surface in the fault zones (Baikal and North Caucasus regions). *Journal of Environmental Radioactivity*, *219*, 106271. https://doi.org/10.1016/j.jenvrad.2020.106271

Mollo, S., Tuccimei, P., Heap, M. J., Vinciguerra, S., Soligo, M., Castelluccio, M., Scarlato, P., & Dingwell, D. B. (2011). Increase in radon emission due to rock failure: An experimental study. *Geophysical Research Letter*, *38*(14), 1–4. https://doi.org/10.1029/2011GL047962

Nicolas, A., Girault, F., Schubnel, F., Pili, É., Passelègue, F., Fortin, J., & Deldicque, D. (2015). Radon emanation from brittle fracturing in granites under upper crustal conditions. *Geophysical Research Letter*, *41*(15), 5436–5443. https://doi.org/10.1002/2014GL061095

Ningxia Bureau of Geology and Mineral Resources (NBGMR). (1989). *Regional geology of Ningxia Hui autonomous region* (pp. 1–196). Geological Publishing House.

Papp, B., Deák, F., Horváth, Á., Kiss, Á., Rajnai, G., & Szabó, C. (2008). A new method for the determination of geophysical parameters by radon concentration measurements in bore-hole. *Journal of Environmental Radioactivity*, *99*(11), 1731–1735. https://doi.org/10.1016/j.jenvrad.2008.05.005

Roeloffs, E. (1999). Earth science: Radon and rock deformation. *Nature*, *399*(6732), 104–105. https://doi.org/10.1038/20072

Sano, Y., Kinoshita, N., Kagoshima, T., Takahata, N., Sakata, S., Toki, T., Kawagucci, S., Waseda, A., Lan, T., Wen, H., Chen, A. T., Lee, H., Yang, T. F., Zheng, G., Tomonaga, Y., Roulleau, E., & Pinti, D. L. (2017). Origin of methane-rich natural gas at the West Pacific convergent plate boundary. *Scientific Reports*, *7*(15646), 1–11. https://doi.org/10.1038/s41598-017-15959-5

Sun, X., Wang, G., Shao, Z., & Si, X. (2016). Geochemical characteristics of emergent gas and groundwater in Haiyuan fault zone. *Earth Science Frontiers*, *23*(3), 140–150.

The Research Group on "Active Fault System around Ordos Massif", State Seismological Bureau (SSB). (1988). *Active fault system around Ordos massif* (pp. 1–335). Seismological Press.

Toutain, J. P., Baubron, J. C., Le-Bronec, J., Allard, P., Briole, P., Marty, B., Miele, G., Tedesco, D., & Luongo, G. (1992). Continuous monitoring

of distal gas emanations at Vulcano, southern Italy. *Bulletin of Volcanology*, *54*(2), 147–155. https://doi.org/10.1007/BF00278004

Tuccimei, P., Mollo, S., Vinciguerra, S., Castelluccio, M., & Soligo, M. (2010). Radon and thoron emission from lithophysae-rich tuff under increasing deformation: An experimental study. *Geophysical Research Letter*, *37*(L05305), 1–5. https://doi.org/10.1029/2009gl042134

Ülküm, Ö., Taşköprü, C., İçhedef, M., Saç, M. M., & Kumru, M. N. (2018). Ground water radon anomalies in Bodrum peninsula. *Terra Nova*, *30*, 152–161. https://doi.org/10.1111/ter.12320

Wang, X., Li, Y., Du, J., & Zhou, X. (2014). Correlations between radon in soil gas and the activity of seismogenic faults in Tangshan area, North China. *Radiation Measurements*, *60*, 8–14. https://doi.org/10.1016/j.radmeas.2013.11.001

Wang, Y., Wang, M., & Shen, Z. K. (2017). Block-like versus distributed crustal deformation around the northeastern Tibetan plateau. *Journal of Asian Earth Sciences*, *140*, 31–47. https://doi.org/10.1016/j.jseaes.2017.02.040

Wesnousky, S. G., Jones, L. M., Scholz, C. H., & Deng, Q. (1984). Historical seismicity and rates of crustal deformation along the margins of the Ordos block, North China. *Bulletin of the Seismological Society of America*, *74*(5), 1767–1783.

Winkler, R., Ruckerbauer, F., & Bunzl, K. (2001). Radon concentration in soil gas: A comparison of the variability resulting from different methods, spatial heterogeneity and seasonal fluctuations. *Science of the Total Environment*, *272*(1), 273–282. https://doi.org/10.1016/s0048-9697(01)00704-5

Working Group of M7. (2012). *Study on the mid-to long-term potential of large earthquakes on the Chinese continent*. Seismological Press.

Xu, S., Zheng, G., Zheng, J., Zhou, S., & Shi, P. (2017). Mantle-derived helium in foreland basins in Xinjiang, Northwest China. *Tectonophysics*, *694*, 319–331. https://doi.org/10.1016/j.tecto.2016.11.015

Yang, Y., Li, Y., Guan, Z. J., Chen, Z., Zhang, L., Lv, C. J., & Sun, F. X. (2018). Correlations between the radon concentrations in soil gas and the activity of the Anninghe and the Zemuhe faults in Sichuan, southwestern of China. *Applied Geochemistry*, *89*, 23–33. https://doi.org/10.1016/j.apgeochem.2017.11.006

Yin, A., & Harrison, T. M. (2000). Geologic evolution of the Himalayan-Tibetan orogen. *Annual Review of Earth and Planetary Sciences*, *28*, 211–280. https://doi.org/10.1146/annurev.earth.28.1.211

Yuce, G., Fu, C. C., D'Alessandro, W., Gulbay, A. H., Lai, C. W., Bellomo, S., Yang, T. F., Italiano, F., & Walia, V. (2017). Geochemical characteristics of soil radon and carbon dioxide within the Dead Sea fault and Karasu fault in the Amik Basin (Hatay), Turkey. *Chemical Geology*, *469*, 129–146. https://doi.org/10.1016/j.chemgeo.2017.01.003

Zhang, Y., Shi, W., & Dong, S. (2019). Neotectonics of North China: Interplay between far-field effect of India-Eurasia collision and Pacific subduction related deep-seated mantle upwelling. *Acta Geologica Sinica*, *93*(5), 3–33.

Zhao, B., Zhang, C., Wang, D., Huang, Y., Tan, K., Du, R., & Liu, J. (2017). Contemporary kinematics of the Ordos block, North China and its adjacent rift systems constrained by dense GPS observations. *Journal of Asian Earth Sciences*, *135*, 257–267. https://doi.org/10.1016/j.jseaes.2016.12.045

Zheng, C., Ding, Z. F., & Song, X. D. (2018). Joint inversion of surface wave dispersion and receiver functions for crustal and uppermost mantle structure beneath the northern north-south seismic zone. *Chinese Journal of Geophysics*, *61*(4), 1211–1224. https://doi.org/10.6038/cjg2018L0443

Zheng, G., Ma, X., Guo, Z., Hilton, D. R., Xu, W., Liang, S., Fan, Q., & Chen, W. (2017). Gas geochemistry and methane emission from Dushanzi mud volcanoes in the southern Junggar Basin, NW China. *Journal of Asian Earth Sciences*, *149*, 184–190. https://doi.org/10.1016/j.jseaes.2017.08.023

Zhou, X., Chen, Z., & Cui, Y. (2016). Environmental impact of CO_2, Rn, Hg degassing from the rupture zones produced by Wenchuan M_S 8.0 earthquake in western Sichuan, China. *Environmental Geochemistry and Health*, *38*(5), 1067–1082. https://doi.org/10.1007/s10653-015-9773-1

Zhu, A., Xie, C., Xu, X., Zhou, Y., Lei, X., & Wang, Y. (2010). Investigation on the possible triggered seismicity in the peripheral areas of the Ordos block by the Wenchuan earthquake. *Earth Science Frontiers*, *17*(5), 206–214.

SUPPORTING INFORMATION

Additional supporting information can be found online in the Supporting Information section at the end of this article.

Data S1.

Figure S3.

Figure S4.

Figure S5.

Table S1.

Table S2.

Table S3.